Mon. Not. R. Astron. Soc. **000**, 1–12 (2016) Printed 31 January 2017 (MN LATEX style file v2.2)

Convective Quenching of Field Reversals in Accretion Disc Dynamos

Matthew S. B. Coleman[1]∗, Evan Yerger[1,2], Omer Blaes[1,3], Greg Salvesen[1]†, and Shigenobu Hirose[4]

[1] *Department of Physics, University of California, Santa Barbara, CA 93106, USA*
[2] *Department of Astrophysical Sciences, Program in Plasma Physics, Princeton, NJ 08540, USA*
[3] *Kavli Institute for Theoretical Physics, University of California, Santa Barbara, CA 93106, USA*
[4] *Department of Mathematical Science and Advanced Technology, Japan Agency for Marine-Earth Science and Technology, Yokohama, Kanagawa 236-0001, Japan*

arXiv:1701.08177v1 [astro-ph.HE] 27 Jan 2017

Accepted —. Received —; in original form —

ABSTRACT

Vertically stratified shearing box simulations of magnetorotational turbulence commonly exhibit a so-called butterfly diagram of quasi-periodic azimuthal field reversals. However, in the presence of hydrodynamic convection, field reversals no longer occur. Instead, the azimuthal field strength fluctuates quasi-periodically while maintaining the same polarity, which can either be symmetric or antisymmetric about the disc midplane. Using data from the simulations of Hirose et al. (2014), we demonstrate that the lack of field reversals in the presence of convection is due to hydrodynamic mixing of magnetic field from the more strongly magnetized upper layers into the midplane, which then annihilate field reversals that are starting there. Our convective simulations differ in several respects from those reported in previous work by others, in which stronger magnetization likely plays a more important role than convection.

Key words: accretion, accretion discs, dynamos, convection — MHD — turbulence — stars: dwarf novae.

1 INTRODUCTION

As a cloud of gas contracts under the influence of gravity, it is likely to reach a point where net rotation dominates the dynamics and becomes a bottleneck restricting further collapse. This scenario naturally leads to a disc structure, thus explaining why accretion discs are so prevalent in astrophysics. The question of how these discs transport angular momentum to facilitate accretion still remains. For sufficiently electrically conducting discs, there is a reasonable consensus that the magnetorotational instability (MRI) is the predominate means of transporting angular momentum, at least on local scales (Balbus & Hawley 1998). There has also been significant work on understanding non-local mechanisms of angular momentum transport, such as spiral waves (Ju et al. 2016). While these global structures may be important in discs with low conductivity, local MRI simulations of fully ionized accretion discs produce values of α consistent with those inferred from observations for accretion discs in binary systems. This is even true for the case of dwarf novae, for which MRI simulations lacking net vertical magnetic flux previously had trouble with matching observations (King et al. 2007; Kotko & Lasota 2012). This is because hydrodynamic convection occurs in the vicinity of the hydrogen ionization regime, and enhances the time-averaged Shakura & Sunyaev (1973) alpha-parameter (Hirose et al. 2014; Hirose 2015). Enhancement of MRI turbulent stresses by convection was also independently claimed by Bodo et al. (2012, 2015). Whether this enhancement is enough to reproduce observed dwarf nova light curves remains an unanswered question, largely due to uncertain physics in the quiescent state and in the propagation of heating and cooling fronts (Coleman et al. 2016).

The precise reason as to why convection enhances the turbulent stresses responsible for angular momentum transport is still not fully understood. Bodo et al. (2012, 2013) conducted simulations with fixed thermal diffusivity and impenetrable vertical boundary conditions, and found that when this diffusivity was low, the time and horizontally-averaged vertical density profiles became very flat or even slightly inverted, possibly due to hydrodynamic convection taking place. They suggested that either these flat profiles, or the overturning convective motions themselves, might make the magnetohydrodynamic dynamo more efficient. Hirose et al. (2014) used radiation MHD simulations with out-

∗ E-mail: mcoleman@physics.ucsb.edu
† NSF Astronomy & Astrophysics Postdoctoral Fellow.

© 2016 RAS

flow vertical boundary conditions, and the hydrogen ionization opacities and equation of state that are relevant to dwarf novae. They found intermittent episodes of convection separated by periods of radiative diffusion. The beginning of the convective episodes were associated with an enhancement of energy in vertical magnetic field relative to the horizontal magnetic energy, and this was then followed by a rapid growth of horizontal magnetic energy. These authors therefore suggested that convection seeds the axisymmetric magnetorotational instability, albeit in a medium that is already turbulent. In addition, the phase lag between stress build up and heating which causes pressure to build up also contributes to an enhancement of the alpha parameter. The mere presence of vertical hydrodynamic convection is not sufficient to enhance the alpha parameter, however; the Mach number of the convective motions also has to be sufficiently high, and in fact the alpha parameter appears to be better correlated with the Mach number of the convective motions than with the fraction of heat transport that is carried by convection (Hirose 2015).

Hydrodynamic convection does not simply enhance the turbulent stress to pressure ratio, however. It also fundamentally alters the character of the MRI dynamo. In the standard weak-field MRI, vertically stratified shearing box simulations exhibit quasi-periodic field reversals of the azimuthal magnetic field (B_y) with periods of ~ 10 orbits (Brandenburg et al. 1995; Davis et al. 2010). These reversals start near the midplane and propagate outward making a pattern (see top-left panel of Figure 1 below) which resembles a time inverse of the solar sunspot butterfly diagram. The means by which these field reversals propagate away from the midplane is likely the buoyant advection of magnetic flux tubes (Gressel 2010), and many studies have also suggested that magnetic buoyancy is important in accretion discs (e.g. Galeev et al. 1979; Brandenburg & Schmitt 1998; Miller & Stone 2000; Hirose et al. 2006; Davis et al. 2010; Blaes et al. 2011). Magnetic buoyancy is consistent with the Poynting flux which tends to be oriented outwards (see top-right panel of Fig. 1), and we give further evidence supporting this theory below. While this explains how field reversals propagate through the disc, it does not explain how these magnetic field reversals occur in the first place, and despite numerous dynamo models there is currently no consensus on the physical mechanism driving the reversals (e.g. Brandenburg et al. 1995; Gressel 2010; Shi et al. 2010, 2016; Squire & Bhattacharjee 2015).

However, in the presence of convection, the standard pattern of azimuthal field reversals is disrupted. Periods of convection appear to be characterized by longer term maintenance of a particular azimuthal field polarity, and this persistent polarity can be of even (Bodo et al. 2015) or odd parity with respect to the disk midplane. As we discuss in this paper, the simulations of Hirose et al. (2014) also exhibit this pattern of persistent magnetic polarity during the intermittent periods of convection, but the field reversals associated with the standard butterfly diagram return during the episodes of radiative diffusion (see Fig. 1 below). Here we exploit this intermittency to try and understand the cause of the persistent magnetic polarity in the convective episodes. We demonstrate that this is due to hydrodynamic mixing of magnetic field from strongly magnetized regions at high altitude back toward the midplane.

This paper is organized as follows. In Section 2 we discuss the butterfly diagram in detail and how it changes character when convection occurs. In Section 3 we describe magnetic buoyancy and the role it plays in establishing the butterfly diagram, and the related thermodynamics. We explain how convection acts to alter these effects in Section 4. The implications of this work are discussed in Section 5, and our results are summarized in Section 6.

2 THE BUTTERFLY DIAGRAM

To construct the butterfly diagram and explore its physical origin, it is useful to define the following quantities related to some fluid variable f: the horizontal average of this quantity, the variation with respect to this horizontal average, and a version of the variable that is smoothed in time over one orbit. These are defined respectively by

$$\langle f \rangle (t,z) \equiv \frac{1}{L_x L_y} \int_{-L_x/2}^{L_x/2} dx \int_{-L_y/2}^{L_y/2} dy f(t,x,y,z) \tag{1a}$$

$$\delta f \equiv f - \langle f \rangle , \tag{1b}$$

$$\{f\}_t (t) \equiv \int_{t-1/2}^{t+1/2} f(t')\, dt' \Big/ 1 \text{ orbit} . \tag{1c}$$

Here L_x, L_y, and L_z are the radial, azimuthal and vertical extents of the simulation domain, respectively (listed in Table 1). Additionally we define the quantity $f_{\rm conv}$ as a means to estimate the fraction of vertical energy transport which is done by convection:

$$f_{\rm conv}(t) \equiv \left\{ \frac{\int \{\langle (e+E)\, v_z \rangle\}_t \, {\rm sign}(z) \, \langle P_{\rm th} \rangle \, dz}{\int \{\langle F_{{\rm tot},z} \rangle\}_t \, {\rm sign}(z) \, \langle P_{\rm th} \rangle \, dz} \right\}_t , \tag{2}$$

where e is the gas internal energy density, E is the radiation energy density, v_z is the vertical velocity, $P_{\rm th}$ is the thermal pressure (gas plus radiation), and $F_{{\rm tot},z}$ is the total energy flux in the vertical direction, including Poynting and radiation diffusion flux. These quantities will assist us in analyzing and discussing the interactions between convection and dynamos in accretion discs.

The butterfly diagram is obtained by plotting $\langle B_y \rangle$ as a function of time and distance from the disc midplane (see left frames of Fig. 1). The radiative simulation ws0429 (from Hirose et al. 2014, and listed in Table 1) shows the standard pattern of field reversals normally associated with the butterfly diagram, which appear to start at the midplane and propagate outwards. This outward propagation of magnetic field is consistent with the Poynting flux (also shown in Fig. 1), which generally points outwards away from the midplane.

When simulations with convection are examined (e.g. ws0446 listed in Table 1), however, the butterfly diagram looks completely different (see bottom left frame of Fig. 1), as first discussed by Bodo et al. (2015). Similar to the lack of the azimuthal magnetic field reversals found by these authors, we find that when convection is present in the Hirose et al. (2014) simulations, there is also a lack of field reversals. Additionally, we find that the azimuthal magnetic field in the high altitude "wings" of the butterfly diagram is better characterized by quasi-periodic pulsations, rather than quasi-periodic field reversals. These pulsations have roughly the same period as the field reversals found in radiative epochs. For example, the convective simulation ws0446

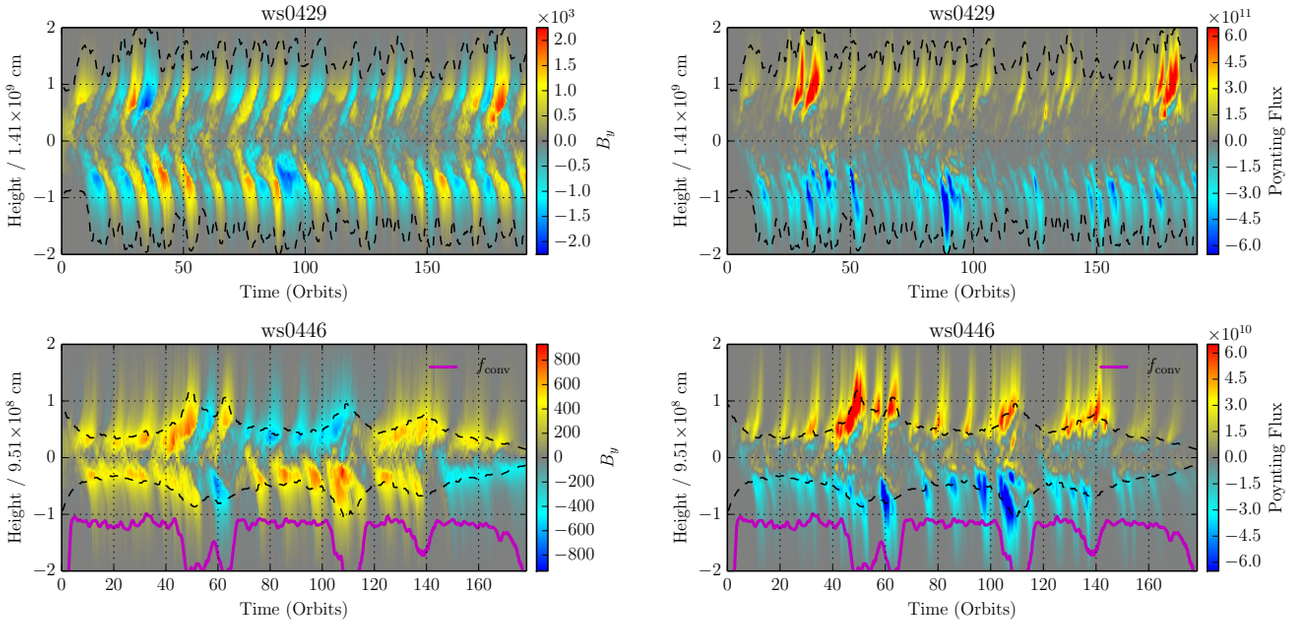

Figure 1. Horizontally-averaged azimuthal magnetic field $\langle B_y \rangle$ (left frames), and 1 orbit smoothed horizontally-averaged vertical Poynting flux $\left\{\langle F_{{\rm Poynt},z}\rangle\right\}_t$ (right frames) as a function of time and height for a radiative simulation (ws0429, top frames) and a simulation which exhibits convective epochs (ws0446, bottom frames). For the Poynting flux frames, we have purposely allowed some of the data to lie outside the colorbar range (which then shows up as saturated regions) in order to increase the color contrast in the midplane regions. The normalizations indicated in the vertical axes are the respective simulation length units. The dashed black lines show the time-dependent heights of the photospheres in the horizontally averaged structures. For simulation ws0446, which exhibits convection, the convective fraction $f_{\rm conv} - 2$ (see Eqn. 2) is plotted in magenta. Note that $f_{\rm conv} - 2$ uses the same vertical scale as B_y, i.e. when the magenta line is near -1 then $f_{\rm conv} \approx 1$. Focusing on B_y, the radiative simulation ws0429 shows the standard pattern of field reversals normally associated with the butterfly diagram. In simulation ws0446 where $f_{\rm conv}$ is high, the field maintains its sign and all changes in sign/parity are associated with a dip in $f_{\rm conv}$.

Simulation	h_0	Σ	$T_{\rm eff}$	α	N_x	N_y	N_z	L_x/h_0	L_y/h_0	L_z/h_0	$L_z/h_{\rm p}$	$t_{\rm th}$
ws0446 (conv)	9.51E+08	127	7490	0.1062	32	64	256	0.500	2.000	4.000	12.0	5.06
ws0429 (rad)	1.41E+09	1030	13352	0.0332	32	64	256	0.500	2.000	4.000	8.54	9.49

Table 1. Simulation parameters for the convective simulation ws0446 and radiative simulation ws0429. The units of time averaged surface densities (Σ), effective temperatures ($T_{\rm eff}$), height (h_0), and thermal time ($t_{\rm th}$) are, respectively, g cm^{-2}, K, cm, and orbits. L_x, L_y, and L_z are the lengths, and N_x, N_y, and N_z are the numbers of cells, in the x, y, and in z directions, respectively. The pressure scale height of the steady state is computed as $h_{\rm p} \equiv \int [\langle p_{\rm thermal}\rangle]\, dz / 2\max([\langle p_{\rm thermal}\rangle])$.

shown in Fig. 1 has a radiative epoch where field reversals occur (centered near 55 orbits), and the behavior of this epoch resembles that of the radiative simulation ws0429. However, during convective epochs where $f_{\rm conv}$ is high, the field maintains its polarity and pulsates with a period of ~ 10 orbits. In fact, the only time field reversals occur is when $f_{\rm conv}$ dips to low values[1], indicating that radiative diffusion is dominating convection.

This lack of field reversals during convective epochs locks the vertical structure of B_y into either an even parity or odd parity state, where B_y maintains sign across the midplane or it changes sign, respectively. (Compare orbits 10-40 to orbits 70-100 in the bottom left panel of Fig. 1). This phenomenon of the parity of B_y being held fixed throughout a convective epoch shall henceforth be referred to as *parity locking*. During even parity epochs (e.g. orbits 10-40 and 120-140 of ws0446), there are field reversals in the midplane, but they are quickly quenched, and what field concentrations are generated here do not migrate away from the midplane as they do during radiative epochs. Also during even parity convective epochs, the Poynting flux tends to be oriented inwards roughly half way between the photospheres and the midplane. For odd parity convective epochs the behavior of the Poynting flux is more complicated but is likely linked to the motion of the $\langle B_y \rangle = 0$ surface.

In summary, we seek to explain the following ways in which convection alters the butterfly diagram:

(i) Magnetic field reversals near the midplane are quickly quenched during convective epochs.

[1] As discussed in Hirose et al. (2014) $f_{\rm conv}$ can be slightly negative. This can happen when energy is being advected inwards to the disc midplane.

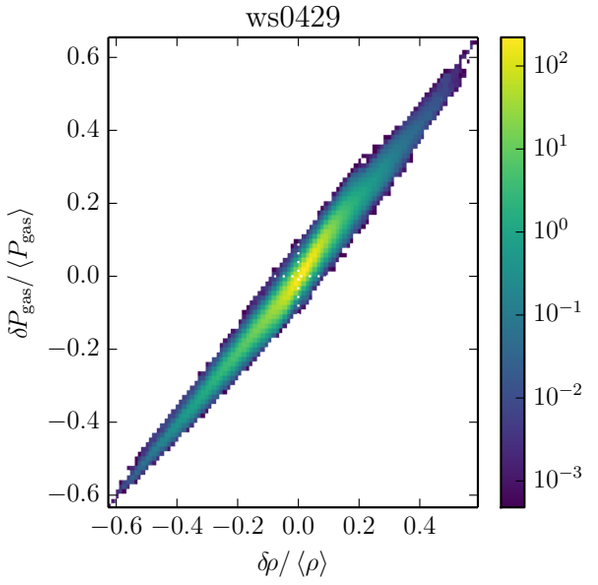

Figure 2. A 2D histogram of horizontal variations (see Eqn. 1b) of mass density ($\delta\rho$, horizontal axis) and gas pressure ($\delta P_{\rm gas}$, vertical axis) for the fully radiative simulation ws0429. Each grid zone saved to file from this simulation with $90 \leqslant t \leqslant 190$ and $|z| \leqslant 0.5$ simulation units is placed into one of 100×100 bins based on its local properties. The resulting normalized probability density is shown here with the given color bar. The probability density, p, is normalized so that $\int p(\tilde{x},\tilde{y})\,d\tilde{x}\,d\tilde{y} = 1$ where $\tilde{x}$ and $\tilde{y}$ are the variables used for the horizontal and vertical axes, respectively. The tight linear correlation between $\delta\rho$ and $\delta P_{\rm gas}$ signifies that temperature variations are small at any fixed height, i.e. horizontal fluctuations are isothermal.

(ii) Magnetic field concentrations do not migrate away from the midplane during convective epochs as they do during radiative epochs.

(iii) During convective epochs, the magnetic field in the wings of the butterfly diagram is better characterized by quasi-periodic pulsations, rather than quasi-periodic field reversals, with roughly the same period.

(iv) B_y is held fixed in either an odd or even parity state during convective epochs.

3 THERMODYNAMICS AND MAGNETIC BUOYANCY

Much like in Blaes et al. (2011), we find that that during radiative epochs, nonlinear concentrations of magnetic field form in the midplane regions, and these concentrations are underdense and therefore buoyant. The resulting upward motion of these field concentrations is the likely cause of the vertically outward moving field pattern observed in the standard butterfly diagram. In our simulations, this magnetic buoyancy appears to be more important when radiative diffusion, rather than convection, is the predominate energy transport process. This is due to the different opacities and rates of radiative diffusion between these two regimes, which alter the thermodynamic conditions of the plasma.

When the disc is not overly opaque, and convection is therefore never present, temperature variations (δT) at a given height are rapidly suppressed by radiative diffusion. This causes horizontal variations in gas pressure ($\delta P_{\rm gas}$) and mass density ($\delta\rho$) to be highly correlated (see Fig. 2), and allows us to simplify our analysis by assuming $\delta T = 0$. This should be contrasted with convective simulations (see Fig. 3) which show a much noisier relation and show a tendency towards adiabatic fluctuations during convective epochs.

By computing rough estimates of the thermal time we can see how isothermal and adiabatic behaviour arise for radiative and convective epochs, respectively. The time scale to smooth out temperature fluctuations over a length scale ΔL is simply the photon diffusion time times the ratio of gas internal energy density e to photon energy density E,

$$t_{\rm th} \simeq \frac{3\kappa_{\rm R}\rho(\Delta L)^2}{c}\frac{e}{E}. \tag{3}$$

For the midplane regions of the radiative simulation ws0429 at times $75-100$ orbits, the density $\rho \simeq 7\times10^{-7}$g cm^{-3}, $e \simeq 2\times10^{7}$ erg cm^{-3}, $E \simeq 9\times10^{5}$ erg cm^{-3}, and the Rosseland mean opacity $\kappa_R \simeq 10$ cm^2 g^{-1}. Hence, $t_{\rm th} \simeq 30(\Delta L/H)^2$ orbits. Radiative diffusion is therefore extremely fast in smoothing out temperature fluctuations on scales of order several tenths of a scale height, and thus horizontal fluctuations are roughly isothermal.

Isothermality ($T = \langle T\rangle$) in combination with pressure equilibrium ($P_{\rm tot} = \langle P_{\rm tot}\rangle$) leads to the following equation:

$$\langle P_{\rm tot}\rangle = \frac{\rho}{\mu m_p}k\,\langle T\rangle + P_{\rm mag}, \tag{4}$$

where radiation pressure has been neglected, as $P_{\rm rad} \ll P_{\rm gas}$. Thus, during radiative epochs, it is clear that regions of highly concentrated magnetic field (e.g. flux tubes) must be under-dense. Figure 4 confirms this for the radiative simulation ws0429 by depicting a 2D histogram of magnetic pressure and density fluctuations. A clear anticorrelation is seen which extends up to very nonlinear concentrations of magnetic field, all of which are underdense. This anticorrelation was also observed in radiation pressure dominated simulations appropriate for high luminosity black hole accretion discs in Blaes et al. (2011). This anti-correlation causes the buoyant rise of magnetic field which would explain the outward propagation seen in the butterfly diagram and is also consistent with the vertically outward Poynting flux (see top panels of Figure 1).

On the other hand, for the midplane regions of the convective simulation ws0446 at the times $80-100$ orbits, $\rho \simeq 2\times10^{-7}$g cm^{-3}, $e \simeq 3\times10^{6}$ erg cm^{-3}, $E \simeq 1\times10^{3}$ erg cm^{-3}, and $\kappa_{\rm R} \simeq 7\times10^{2}$ cm^2 g^{-1}. Hence, $t_{\rm th} \simeq 4\times10^{4}(\Delta L/H)^2$ orbits. All fluctuations in the midplane regions that are resolvable by the simulation are therefore roughly adiabatic. Perhaps somewhat coincidentally, $\Gamma_1 \approx 1.3$ in the midplane regions of the convective simulation, so the pressure-density fluctuations, even though adiabatic, are in any case close to an isothermal relationship[2]. However, the biggest difference between the radiative and convective cases is caused

[2] This reduction in the adiabatic gradient within the hydrogen ionization transition actually contributes significantly to establishing a convectively unstable situation in our dwarf nova simulations. We typically find that the adiabatic temperature gradient $\nabla_{\rm ad}$ within the hydrogen ionization transition is significantly less than the value 0.4 for a monatomic gas. In fact, the gas pressure

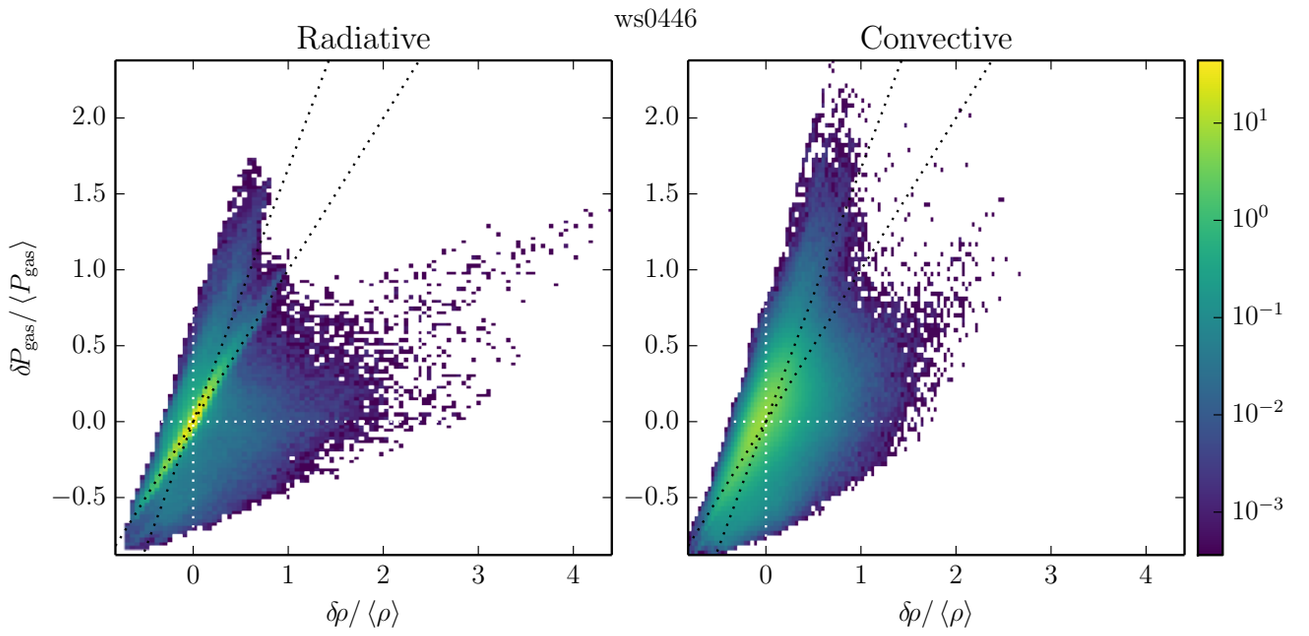

Figure 3. 2D histograms of horizontal variations of mass density ($\delta\rho$, horizontal axis) and gas pressure ($\delta P_{\rm gas}$, vertical axis) in the convective simulation ws0446. The left panel shows data from a radiative epoch ($49 \leqslant t \leqslant 64$), and the right panel shows data from a convective epoch ($70 \leqslant t \leqslant 100$). The two dotted black lines in each figure show the expected relations for isothermal (slope 1) and monatomic adiabatic (slope 5/3) gases. During the radiative epoch there is a significant population of cells that lie on the line $\delta P_{\rm gas} = \delta\rho$ just as in Fig. 2. However there is also a significant amount of dispersion which resembles the probability distribution of the convective epoch, therefore it is likely that this dispersion is a remnant of the previous convective epoch. During the convective epoch the yellow core of the probability distribution follows a linear trend with a slope steeper than 1. This is indicative of perturbations which are adiabatic and the spread in slopes over this yellow region are likely due to the variation in $\Gamma_1 \equiv (\partial \ln P_{\rm gas}/\partial \ln \rho)_s$ from our equation of state, which includes in particular the effects of ionizing hydrogen. Values of Γ_1 range from about 1.15 to 5/3 in this simulation. The population below $\delta P_{\rm gas} = \delta\rho$ is likely a result of vertical mixing.

by the departure from isothermality in convective epochs, allowing for the possibility of highly magnetized regions to be overdense. This leads to much larger scatter in the probability distribution of the density perturbations in convective epochs. How this affects magnetic buoyancy in radiative and convective epochs will be discussed in detail in the next section.

4 EFFECTS OF CONVECTION

In this section we lay out the main mechanisms by which convection acts to modify the dynamics of the dynamo and thereby fundamentally alter the large scale magnetic field structure in the simulations.

4.1 Mixing from the Wings

As a convective cell brings warm underdense plasma from the midplane outward towards the photosphere (i.e. the wing region of the butterfly diagram), it must also circulate cold overdense material from the wing down towards the midplane. As is typical of stratified shearing box simulations of MRI turbulence (e.g. Miller & Stone 2000; Krolik et al. 2007), the horizontally and time-averaged magnetic energy density peaks away from the midplane, and the surface photospheric regions are magnetically dominated. Dense fluid parcels that sink down toward the midplane are therefore likely to carry significant magnetic field inward. These fluid parcels that originated from high altitude can actually be identified in the simulations because the high opacity, which contributes to the onset of convection, prevents cold fluid parcels from efficiently thermalizing with their local surroundings. Hence they retain a lower specific entropy compared to their surroundings as they are brought to the midplane by convective motions. We therefore expect negative specific entropy fluctuations in the midplane regions to be correlated with high azimuthal magnetic field strength of the same polarity as the photospheric regions during a convective epoch. Figures 5 and 6 show that this is indeed the case.

Figure 5 shows a 2D histogram of entropy fluctuations and azimuthal field strength B_y in the midplane regions for the even parity convective epoch $15 \leqslant t \leqslant 40$ in simulation ws0446 (see Fig. 1). The yellow vertical population is indicative of adiabatic fluctuations (i.e. $\delta s = 0$) at every height which are largely uncorrelated with B_y. However, the upper left quadrant of this figure shows a significant excess of

weighted average value of $\nabla_{\rm ad}$ can be as low as 0.18. For $\sim 60\%$ of the convective simulations of Hirose et al. (2014) and Coleman et al. (2016), the temperature gradient ∇ is superadiabatic but less than 0.4 during convective epochs.

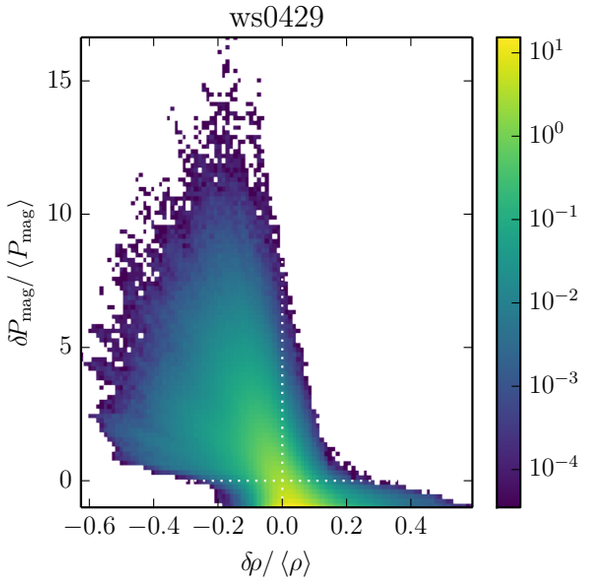

Figure 4. A 2D histogram of horizontal variations of mass density ($\delta\rho$, horizontal axis) and magnetic pressure ($\delta P_{\rm mag}$, vertical axis), using data from the same vertical and temporal ranges as Fig. 2. The rough anti-correlation between $\delta\rho$ and $\delta P_{\rm mag}$ signifies that highly magnetized regions are likely to be underdense and thus buoyant.

cells with lower than average entropy for their height and large positive B_y. It is important to note that this corresponds to the sign of the azimuthal field at high altitude, even though near the midplane $\langle B_y\rangle$ is often negative (see bottom panel of Fig. 1). This is strong evidence that convection is advecting low entropy magnetized fluid parcels from the near-photosphere regions into the midplane.

Figure 6 shows the same thing for the odd parity convective epoch $80 \leqslant t \leqslant 100$. Because the overall sign of the horizontally-averaged azimuthal magnetic field flips across the midplane, cells that are near but above the midplane are shown in the left panel, while cells that are near but below the midplane are shown on the right. Like in Figure 5, there is a significant excess of negative entropy fluctuations that are correlated with azimuthal field strength and have the same sign as the field at higher altitudes *on the same side of the midplane*. Again, these low entropy regions represent fluid parcels that have advected magnetic field inward from higher altitude. The correlation between negative entropy fluctuation and azimuthal field strength is somewhat weaker than in the even parity case (Fig. 5), but that is almost certainly due to the fact that inward moving fluid elements can overshoot across the midplane.

In contrast, Figure 7 shows a similar histogram of entropy fluctuations and B_y for the radiative simulation ws0429, and it completely lacks this correlation between high azimuthal field strength and negative entropy fluctuation. This is in part due to the fact that fluid parcels are no longer adiabatic, but isothermal. But more importantly, it is because there is no mixing from the highly magnetized regions at high altitude down to the midplane. Instead, the tight crescent shaped correlation of Figure 7 arises simply by considering the linear theory of isothermal, isobaric fluctuations at a particular height. Such fluctuations have perturbations in entropy given by

$$\delta s = \frac{k}{\mu m_p}\frac{B^2 - \langle B^2\rangle}{2\langle P_{\rm gas}\rangle}. \tag{5}$$

This is shown as the dotted line in Figure 7, and fits the observed correlation very well.

The inward flux of magnetic energy from high altitude is also energetically large enough to quench field reversals in the midplane regions. To demonstrate this, we examined the divergence of the Poynting flux and compared it to the time derivative of the magnetic pressure. During radiative epochs when the magnetic field is growing after a field reversal, typical values for $\mathrm{d}\langle P_{\rm mag}\rangle/\mathrm{d}t$ in the midplane are about half of the typical value of $-\mathrm{d}\langle F_{{\rm Poynt},z}\rangle/\mathrm{d}z$ near the midplane during convective epochs. This shows that the magnetic energy being transported by the Poynting flux during convective epochs is strong enough to quench the field reversals that would otherwise exist. The sign of the divergence of the Poynting flux during convective epochs is also consistent with magnetic energy being removed from high altitude (positive) and deposited in the midplane (negative).

To conclude, by using specific entropy as a proxy for where a fluid parcel was last in thermal equilibrium, we have shown that convection advects field inward from high altitude, which is consistent with the inward Poynting flux seen during even parity convective epochs (see Fig. 1). The lack of such clear inward Poynting flux during the odd parity convective epochs is likely related to the movement of the $\langle B_y\rangle = 0$ surface by convective overshoot across the disc midplane. However, in both even and odd convective epochs $\mathrm{d}\langle F_{{\rm Poynt},z}\rangle/\mathrm{d}z$ is typically a few times $\mathrm{d}\langle P_{\rm mag}\rangle/\mathrm{d}t$ and is consistent with enough magnetic energy being deposited in the midplane to quench field reversals that would otherwise take place. This further suggests that regardless of parity, this convective mixing from high altitude to the midplane is quenching field reversals in the midplane by mixing in field of a consistent polarity.

4.2 Disruption of Magnetic Buoyancy

In addition to quenching magnetic field reversals, convection and the associated high opacities act to disrupt magnetic buoyancy which transports field away from the midplane, thereby preventing any reversals which do occur, from propagating vertically outwards. The large opacities which contribute to the onset of convection also allow for thermal fluctuations on a given horizontal slice (δT) to persist for several orbits. This breaks one of the approximations which lead to the formulation of Eqn. 4, allowing for the possibility for large magnetic pressures to be counterbalanced by low temperatures, reducing the anti-correlation between density and temperature. Additionally, convective turbulence also generates density perturbations that are uncorrelated with magnetic fields, and combined with the lack of isothermality can cause fluid parcels to have both a high magnetic pressure and be overdense (see Fig. 8). These overdense over-magnetized regions can be seen in the right (convective) frame of Fig. 8 where the probability density at $\delta\rho \approx 0.5\langle\rho\rangle$, $\delta P_{\rm mag} \approx \langle P_{\rm mag}\rangle$ is only about one order

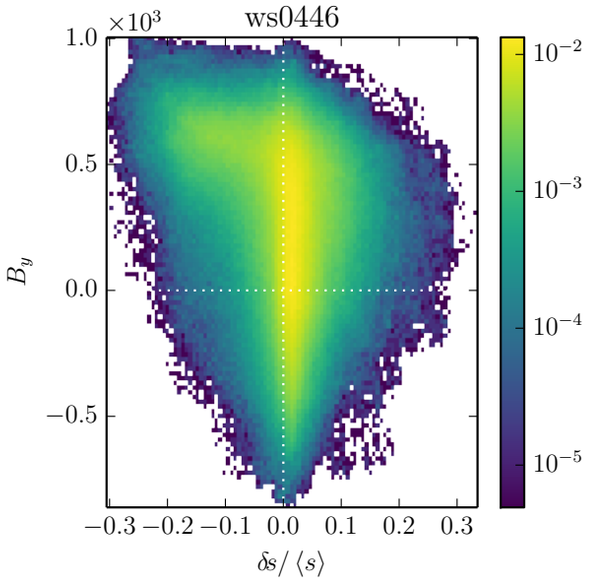

Figure 5. A 2D histogram of azimuthal magnetic field (B_y, vertical axis) and horizontal variations of specific entropy (δs, horizontal axis) for an even parity convective epoch. Each cell saved to file from ws0446 with $15 \leqslant t \leqslant 40$ and $|z| \leqslant 0.25$ simulation units is placed into one of 100×100 bins based on its local properties. The light green region at low entropy ($-0.2 \lesssim \delta s < 0$) and high magnetic field ($B_y \gtrsim 500$) signifies highly magnetized fluid parcels which have been mixed towards the midplane by convection.

of magnitude below its peak value. This should be contrasted with the left (radiative) frame of the same figure and with Fig. 4 where the probability density at this coordinate is very small or zero respectively. Hence while the overall anti-correlation between magnetic pressure and density still exists in convective epochs, indicating some magnetic buoyancy, the correlation is weakened by the presence of overdense high magnetic field regions. Magnetic buoyancy is therefore weakened compared to radiative epochs.

4.3 Parity Locking

The effects described above both prevent magnetic field reversals in the midplane and reduce the tendency for any reversals which manage to occur from propagating outwards. Therefore convection creates an environment which prevents field reversals, and leads to the parity of the field being locked in place. Due to the variety of parities seen, it appears likely that it is simply the initial conditions when a convective epoch is initiated that set the parity for the duration of that epoch.

5 DISCUSSION

It is important to note that we still do not understand many aspects of the MRI turbulent dynamo. Our analysis here has not shed any light on the actual origin of field reversals in the standard (non-convective) butterfly diagram, nor have we provided any explanation for the quasi-periodicities observed in both the field reversals of the standard diagram and the pulsations that we observe at high altitude during convective epochs. However, the outward moving patterns in the standard butterfly wings combined with the fact that the horizontally-averaged Poynting flux is directed outward strongly suggests that field reversals are driven in the midplane first and then propagate out by magnetic buoyancy. On the other hand, we continue to see the same quasi-periodicity at high altitude in convective epochs as we do in the field reversals in the radiative epochs. Moreover, it is clear from Figure 1 that field reversals occasionally start to manifest in the midplane regions during convective epochs, but they simply cannot be sustained because they are annihilated by inward advection of magnetic field of sustained polarity. This suggests perhaps that there are two spatially separated dynamos which are operating. This modification of the dynamo by convection presents a challenge to dynamo models. However, potentially promising dynamo mechanisms have recently been discovered in stratified and unstratified shearing boxes.

Recently, Shi et al. (2016) found that quasi-periodic azimuthal field reversals occur even in unstratified, zero net flux shearing box simulations, provided they are sufficiently tall ($L_z/L_x \geqslant 2.5$). Furthermore, they found that the magnetic shear-current effect (discussed in Squire & Bhattacharjee 2015) was responsible for this dynamo; however, they were not able to explain why the reversals occurred. The shear-current effect can also apparently be present during hydrodynamic convection (Rogachevskii & Kleeorin 2007), implying that this dynamo mechanism might be capable of persisting through convective epochs.

Most of the work on the MRI dynamo has been done with vertically stratified shearing box simulations. One of the earliest examples of this is Blackman & Tan (2004), who found that multiple dynamos can work in conjunction with the MRI on different scales. This is consistent with the findings of Gressel (2010), that an "indirect" larger scale dynamo should coexist with the MRI, and they propose two candidates: a Parker-type dynamo (i.e. the α-effect; Parker 1955; Ruediger & Kichatinov 1993), and a "buoyant" dynamo caused by the Lorentz force. Furthermore, Gressel & Pessah (2015) find that the $\alpha\Omega$ dynamo produces cycle frequencies comparable to that of the butterfly diagram, and that there is a non-local relation between electromotive forces and the mean magnetic field which varies vertically throughout the disc. This sort of non-local description may be necessary to understand how the midplane and high altitude regions differ from each other, and we hope to pursue such an analysis in future work.

5.1 Departures from Standard Disc Dynamo: Comparison with Other Works

We find that some properties of the dynamo during convective epochs are similar to the convective simulations of Bodo et al. (2012, 2015), such as prolonged states of azimuthal magnetic field polarity and an enhancement of Maxwell stresses compared to purely radiative simulations (see, e.g. Figure 6 of Hirose et al. 2014). However, there are some dynamo characteristics observed by Bodo et al. (2015) that are not present in our simulations. For example,

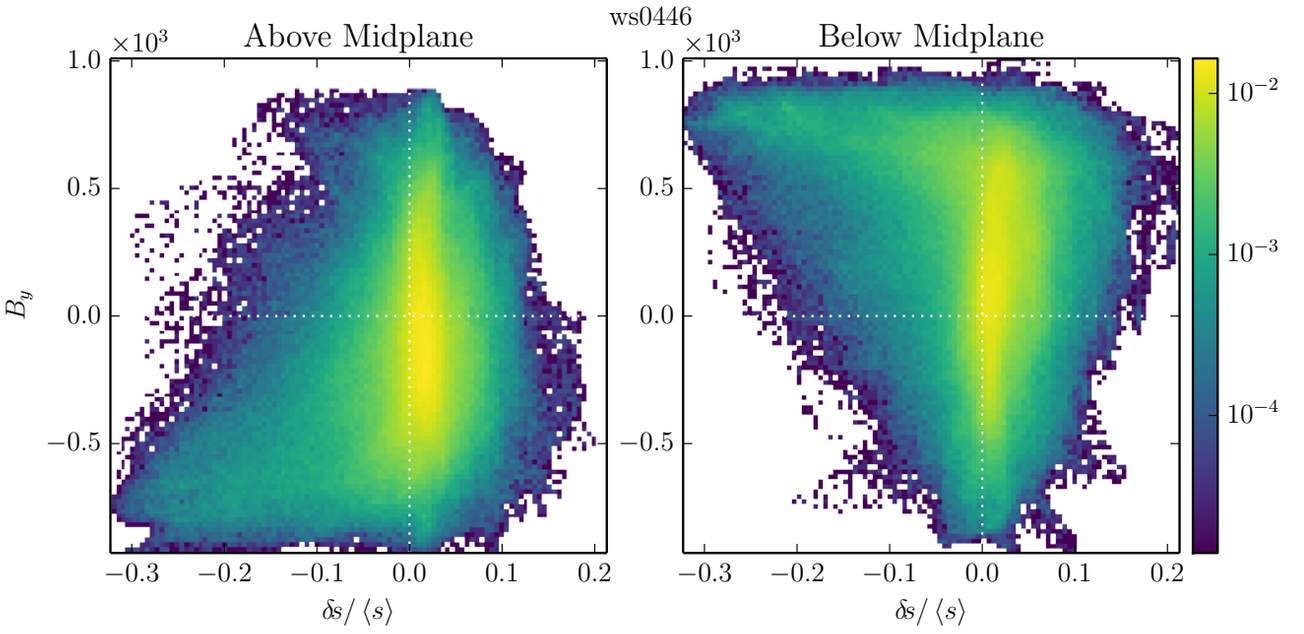

Figure 6. 2D histograms of azimuthal magnetic field (B_y, vertical axis) and horizontal variations of specific entropy (δs, horizontal axis). Each cell saved to file from ws0446 with $80 \leqslant t \leqslant 100$ and $0 \leqslant z \leqslant 0.25$ simulation units (left) and $-0.25 \leqslant z \leqslant 0$ simulation units (right) are used to create the respective histograms. It is important to note that for both panels there is a low entropy, high $|B_y|$ tail which corresponds to the sign of the respective wings of the butterfly diagram (see bottom panel of Fig. 1), indicating that convection is mixing regions of high magnetization from the wings into the midplane.

their simulations typically evolved to a strongly magnetized state, something which we never find. We also find that in our simulations, which exhibit intermittent convection, the time-averaged Maxwell stress in the midplane regions is approximately the same in both the convective and radiative epochs[3], and is independent of the vertical parity of the azimuthal field. In contrast, Bodo et al. (2015) find substantially less Maxwell stress during odd parity epochs. Azimuthal field reversals occasionally occur during their convective simulations, whereas we never see such reversals during our convective epochs. Finally, their simulations exhibit a strong preference for epochs of even parity, and a lack of quasi-periodic pulsations in the wings of the butterfly diagram.

Remarkably, all of these aforementioned properties of their simulations arise in strongly magnetized shearing box simulations (Bai & Stone 2013; Salvesen et al. 2016b). We suggest here that these properties of the dynamo that Bodo et al. (2015) attribute to convection are actually a manifestation of strong magnetization. To demonstrate this, we start by noting that the simulations presented in Bodo et al. (2015) adopted: (1) impenetrable vertical boundary conditions that prevented outflows; thus, trapping magnetic field within the domain, and (2) initial configurations with either zero or non-zero net vertical magnetic flux.

[3] Although the Maxwell stress is approximately the same between radiative and convective epochs in a given simulation, the α parameter is enhanced during convective epochs because the medium is cooler and the time-averaged midplane pressure is smaller.

We first consider the Bodo et al. (2015) simulations with net vertical magnetic flux. Figure 10 of Bodo et al. (2015) shows that for increasing net vertical flux, the strength of the azimuthal field increases and field reversals decrease in frequency with long-lived (short-lived/transitionary) epochs of even (odd) parity. No dynamo flips in the azimuthal field were seen for the strongest net flux case. Figure 9 shows that the *isothermal* net vertical flux simulations of Salvesen et al. (2016b) reproduce all features of the butterfly diagrams in the convective simulations of Bodo et al. (2015), for the same range of initial plasma-β. This remarkable similarity between these simulations with and without convective heat transport suggests that strong magnetization (i.e., $\beta \sim 1$ at the disc mid-plane) is responsible for the conflicts listed in the previous paragraph with the Hirose et al. (2014) simulations under consideration.

We now seek to understand the role of convection on dynamo behavior in the zero net vertical magnetic flux simulations of Bodo et al. (2015). These simulations also developed into a strongly magnetized state and exhibited similarly dramatic departures from the standard butterfly pattern as their net flux counterparts. Gressel (2013) demonstrated that zero net vertical flux shearing box simulations with constant thermal diffusivity and the same impenetrable vertical boundaries adopted by Bodo et al. (2015) lead to the following: (1) A butterfly pattern that is irregular, yet still similar to the standard pattern that is recovered for outflow boundaries. However, the box size in Gressel (2013) was comparable to the smallest domain considered in Bodo et al. (2015), which was not a converged solution. (2) Maxwell stresses that are enhanced by a factor of ~ 2 compared to the simulation with outflow boundaries. This

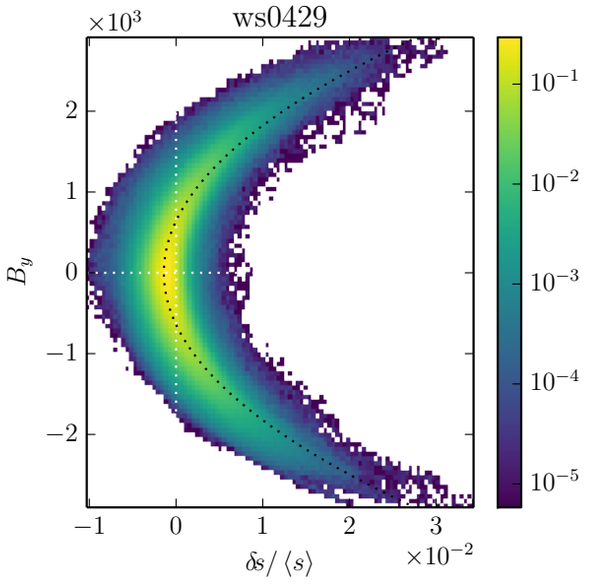

Figure 7. A 2D histogram of azimuthal magnetic field (B_y, vertical axis) and horizontal variations of specific entropy (δs, horizontal axis) for the radiative simulation ws0429. Note the symmetry and how the probability distribution curves to high entropy at high magnetic field strength. This curvature is indicative of isothermal, isobaric fluctuations and matches well with linear theory (black dotted line) which is computed from Eqn. 5 assuming that $B^2 = B_y^2$. This trend should be contrasted with what we observe during convective epochs in Figs. 5 and 6. Note that the entropy fluctuations here are an order of magnitude smaller compared to those of the convective simulation ws0446.

is likely because impenetrable boundaries confine magnetic field, which would otherwise buoyantly escape the domain (Salvesen et al. 2016a). (3) Substantial turbulent convective heat flux, which is significantly reduced when using outflow boundaries. Therefore, perhaps the enhanced convection resulting from using impenetrable boundaries is indeed responsible for the strongly magnetized state and dynamo activity seen in the "Case D" zero net flux simulation of Bodo et al. (2015).

Despite starting with identical initial and boundary conditions, the zero net vertical flux simulation M4 of Gressel (2013) does not evolve to the strongly magnetized state seen in the Bodo et al. (2015) simulations. The reason for this discrepancy is unclear. In an attempt to reproduce Case D in Bodo et al. (2015) and following Salvesen et al. (2016a), we ran an *isothermal*, zero net vertical flux shearing box simulation that had an initial magnetic field, $\mathbf{B} = B_0 \sin(2\pi x/L_x)$, where B_0 corresponded to $\beta_0 = 1600$. This simulation, labeled ZNVF-βZ1600, had domain size $(L_x, L_y, L_z) = (24H_0, 18H_0, 6H_0)$ with H_0 being the initial scale height due to thermal pressure support alone, resolution 24 zones/H_0 in all dimensions, and periodic vertical boundaries that trap magnetic field, which we believe to be the salient feature of the impenetrable boundaries discussed above. Figure 10 shows that the space-time diagram of the horizontally-averaged azimuthal magnetic field for this simulation does not reproduce Case D, but instead evolves to a weakly magnetized state with a conventional butterfly pattern.

However, we note that Gressel (2013) found that the standard butterfly diagram is recovered when replacing impenetrable boundaries with outflow boundaries. Similarly, Salvesen et al. (2016a) initialized two zero net vertical flux simulations with a purely azimuthal magnetic field corresponding to $\beta_0 = 1$. In simulation ZNVF-P, which adopted periodic boundary conditions that prevent magnetic field from buoyantly escaping, the butterfly pattern was not present and the azimuthal field locked into a long-lived, even parity state. However, for simulation ZNVF-O, which adopted outflow vertical boundaries, the initially strong magnetic field buoyantly escaped and the disc settled down to a weakly magnetized configuration with the familiar dynamo activity (see Figure 2 of Salvesen et al. 2016a). Therefore, vertical boundaries that confine magnetic field may dictate the evolution of shearing box simulations without net poloidal flux.

Based on the discussion above, we suggest that the dynamo behavior in the Bodo et al. (2015) simulations with net vertical magnetic flux is a consequence of strong magnetization and not convection. For the zero net vertical flux simulations with impenetrable vertical boundaries, the relative roles of convection *vs.* strong magnetization in influencing the dynamo is less clear. The main result of this paper — that convection quenches azimuthal field reversals in accretion disc dynamos — applies to the case of zero net vertical magnetic flux and realistic outflow vertical boundaries. Future simulations in this regime with larger domain size will help to determine the robustness of this result.

5.2 Quasi-Periodic Oscillations

In addition to the outburst cycles observed in dwarf novae, cataclysmic variables in general exhibit shorter timescale variability such as dwarf nova oscillations (DNOs) on ~ 10 s time scales and quasi-periodic oscillations (QPOs) on $\sim$ minute to hour time scales (Warner 2004). A plausible explanation for DNOs in CVs involving the disk/white dwarf boundary layer has been proposed (Woudt & Warner 2002; Warner & Woudt 2002). However, a substantial number of QPOs remain unexplained. It is possible that the quasi-periodic magnetic field reversals seen in the MRI butterfly diagram are responsible for some of these QPOs and other variability. Temporally, one would expect variations from the butterfly diagram to occur on minutes to an hour timescales:

$$\tau_{\rm bf} = 223\,{\rm s} \times r_9^{3/2} \left(\frac{M}{0.6\,M_\odot}\right)^{-1/2} \frac{\tau_{\rm bf}}{10\,\tau_{\rm orb}}, \qquad (6)$$

where $\tau_{\rm bf}$ is the period of the butterfly cycle, r_9 is the radial location of variability in units of 10^9 cm, M is the mass of the white dwarf primary, and $\tau_{\rm orb}$ is the orbital period.

Indeed, this suggestion has already been made in the context of black hole X-ray binaries (O'Neill et al. 2011; Salvesen et al. 2016b), however, no plausible emission mechanism to convert these field reversals into radiation has been identified. However, it is noteworthy that quasi-periodic azimuthal field reversals have also been seen in global accretion disk simulations with substantial coherence over broad ranges of radii (e.g. O'Neill et al. 2011; Flock et al. 2012; Jiang et al. 2014), indicating that this phenomena is not

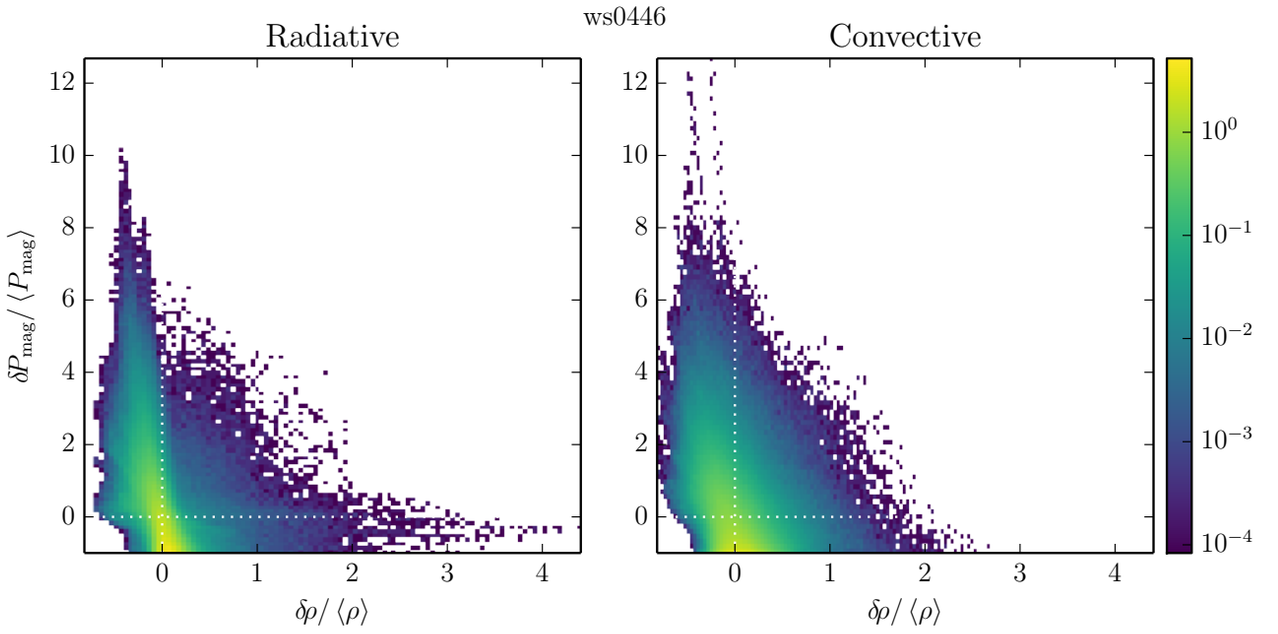

Figure 8. 2D histograms of horizontal variations of mass density ($\delta\rho$, horizontal axis) and magnetic pressure ($\delta P_{\rm mag}$, vertical axis). The left panel shows data from a radiative epoch ($49 \leqslant t \leqslant 64$) of simulation ws0446 and the right panel shows data from a convective epoch ($70 \leqslant t \leqslant 100$) of the same simulation. While there is still a rough anti-correlation between $\delta\rho$ and $\delta P_{\rm mag}$ as seen in Fig. 4 this correlation is much weaker here. Also, note that the scale of the x-axis here is an order of magnitude higher than that of Fig. 4. The left frame is similar to the data from ws0429 but has an extra source of dispersion which is likely connected to previous episodes of convection. The right frame has a significantly higher population of overdense and highly magnetized fluid parcels compared to the radiative epoch. This signifies that magnetic buoyancy is weakened during convective epochs.

unique to shearing box simulations. If QPOs in dwarf novae are in fact associated with azimuthal field reversals, then our work here further suggests that these QPOs will differ between quiescence and outburst due to the fact that the convection quenching of field reversals (i.e. the butterfly diagram) only occurs in outburst, and this quenching may leave an observable mark on the variability of dwarf novae.

6 CONCLUSIONS

We analyzed the role of convection in altering the dynamo in the shearing box simulations of Hirose et al. (2014). Throughout this paper we explained how convection acts to:

(i) quickly quench magnetic field reversals near the midplane;
(ii) weaken magnetic buoyancy which transports magnetic field concentrations away from the midplane;
(iii) prevent quasi-periodic field reversals, leading to quasi-periodic pulsations in the wings of the butterfly diagram instead; and
(iv) hold the parity of B_y fixed in either an odd or even state.

All of these are dramatic departures from how the standard quasi-periodic field reversals and resulting butterfly diagram work during radiative epochs.

The primary role of convection in disrupting the butterfly diagram is to mix magnetic field from high altitude (the wings) down into the midplane. This mixing was identified through correlations between entropy and B_y (see Figs. 5, 6). Due to the high opacity of the convective epochs, perturbed fluid parcels maintain their entropy for many dynamical times. Hence the observed low-entropy highly-magnetized fluid parcels found in the midplane must have been mixed in from the wings. The sign of B_y for these parcels also correspond to the wing which is closest and tend to oppose the sign found in the midplane, quenching field reversals there.

The high opacity which allows for the fluid parcels to preserve their entropy also allows for thermal fluctuations to be long lived. This combined with the turbulence generated by convection weakens the anti-correlation between magnetic pressure and density found in radiative simulations (contrast Figs. 4 and 8) and creates an environment where some flux tubes can be overdense. This acts to weaken, but not quench, magnetic buoyancy thereby preventing the weak and infrequent field reversals which do occur from propagating outwards to the wings.

It is through these mechanisms that convection acts to disrupt the butterfly diagram and prevent field reversals, even though it is clear that the MRI turbulent dynamo continues to try and drive field reversals in the midplane regions. This results in the sign of B_y and its parity across the midplane to be locked in place for the duration of a convective epoch. The quenching of field reversals and the maintenance of a particular parity (odd or even) across the midplane is a hallmark of convection in our simulations, and we hope that it may shed some light on the behaviour of the MRI turbulent dynamo in general.

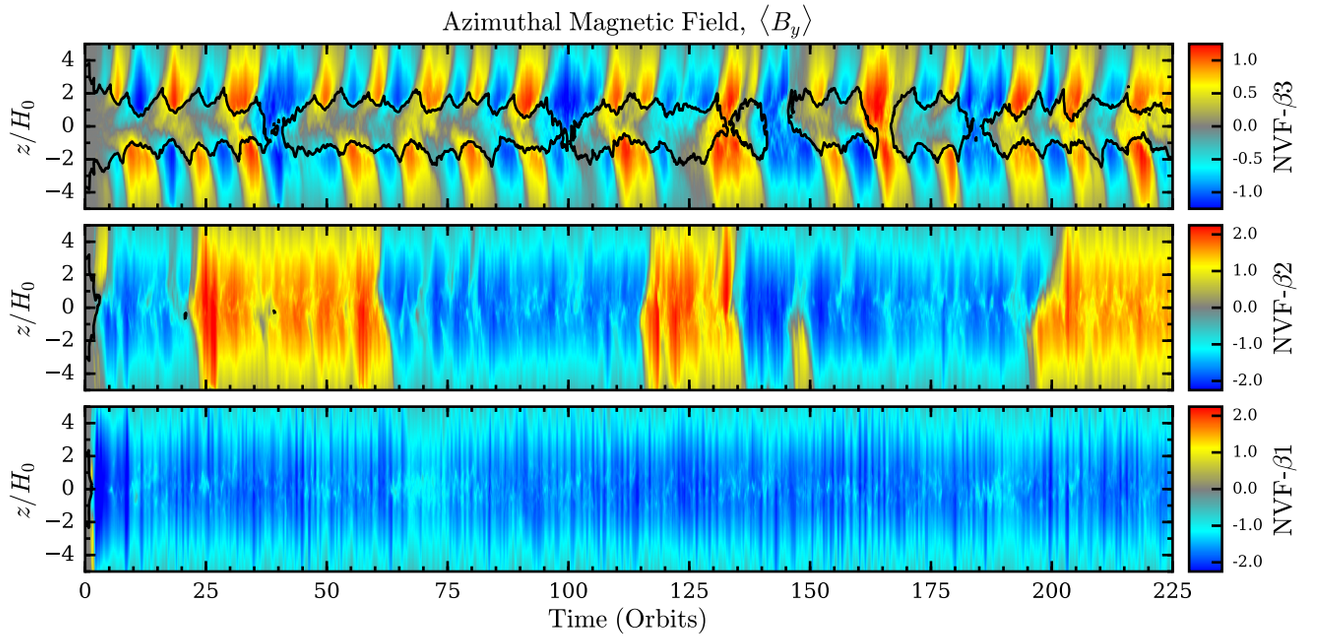

Figure 9. Vertical profiles of the horizontally-averaged azimuthal magnetic field for isothermal shearing box simulations with different levels of net vertical magnetic flux corresponding to an initial mid-plane plasma-β of: $\beta_0^{\rm mid} = 1000$ (*top*), $\beta_0^{\rm mid} = 100$ (*middle*), $\beta_0^{\rm mid} = 10$ (*bottom*). *Black lines* in the top panel mark the $\beta = 1$ contour and are absent in the bottom two panels because $\beta < 1$ throughout the entire vertical column. For these simulations and the net vertical flux simulations considered by Bodo et al. (2015) where $\beta_0^{\rm mid} \lesssim 1000$, the entire disc becomes strongly magnetized (i.e., $\beta \lesssim 1$ everywhere). The butterfly patterns seen in the convective net vertical flux simulations in Figure 10 of Bodo et al. (2015) bears a striking resemblance to these isothermal simulations, which do not have convective heat transport. This is suggestive that the dramatic departure from the usual butterfly pattern seen in the net flux simulations of Bodo et al. (2015) is due to strong magnetization. (This figure is reproduced from Salvesen et al. 2016b.)

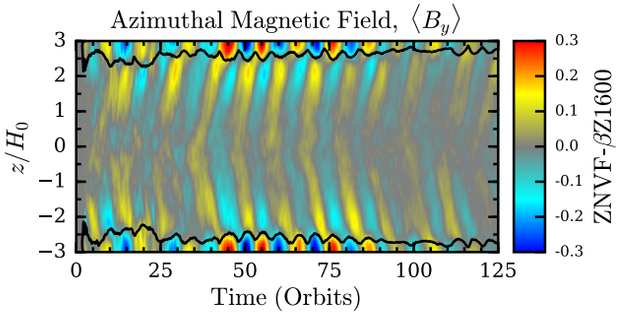

Figure 10. Vertical profile of the horizontally-averaged azimuthal magnetic field for the isothermal, zero net vertical flux shearing box simulation ZNVF-β1600, which was designed to reproduce the Case D simulation of Bodo et al. (2015). Unlike Case D, the ZNVF-β1600 simulation displays the standard butterfly pattern and does not develop strong magnetization. We note that the Gressel (2013) simulations with finite thermal diffusivity also did not generate dynamically important magnetic fields.

ACKNOWLEDGEMENTS

We thank the anonymous referee for a constructive report that led to improvements in this paper. We also wish to acknowledge Tobias Heinemann, Amitiva Bhattacharjee, and Johnathan Squire for their useful discussions and insight generated from their work. This research was supported by the United States National Science Foundation under grant AST-1412417 and also in part by PHY11-25915. We also acknowledge support from the UCSB Academic Senate, and the Center for Scientific Computing from the CNSI, MRL: an NSF MRSEC (DMR-1121053) and NSF CNS-0960316. SH was supported by Japan JSPS KAKENH 15K05040 and the joint research project of ILE, Osaka University. GS is supported by an NSF Astronomy and Astrophysics Postdoctoral Fellowship under award AST-1602169. Numerical calculation was partly carried out on the Cray XC30 at CfCA, National Astronomical Observatory of Japan, and on SR16000 at YITP in Kyoto University. This work also used the Janus supercomputer, which is supported by the National Science Foundation (award number CNS-0821794) and the University of Colorado Boulder. The Janus supercomputer is a joint effort of the University of Colorado Boulder, the University of Colorado Denver, and the National Center for Atmospheric Research.

REFERENCES

Bai, X.-N., & Stone, J. M. 2013, ApJ, 767, 30
Balbus, S. A., & Hawley, J. F. 1998, Reviews of Modern Physics, 70, 1
Blackman, E. G., & Tan, J. C. 2004, Astrophys. Space Sci., 292, 395
Blaes, O., Krolik, J. H., Hirose, S., & Shabaltas, N. 2011, ApJ, 733, 110

Bodo, G., Cattaneo, F., Mignone, A., & Rossi, P. 2012, ApJ, 761, 116
—. 2013, ApJ, 771, L23
—. 2015, ApJ, 799, 20
Brandenburg, A., Nordlund, A., Stein, R. F., & Torkelsson, U. 1995, ApJ, 446, 741
Brandenburg, A., & Schmitt, D. 1998, A&A, 338, L55
Coleman, M. S. B., Kotko, I., Blaes, O., Lasota, J.-P., & Hirose, S. 2016, MNRAS, 462, 3710
Davis, S. W., Stone, J. M., & Pessah, M. E. 2010, ApJ, 713, 52
Flock, M., Dzyurkevich, N., Klahr, H., Turner, N., & Henning, T. 2012, ApJ, 744, 144
Galeev, A. A., Rosner, R., & Vaiana, G. S. 1979, ApJ, 229, 318
Gressel, O. 2010, MNRAS, 405, 41
—. 2013, ApJ, 770, 100
Gressel, O., & Pessah, M. E. 2015, ApJ, 810, 59
Hirose, S. 2015, MNRAS, 448, 3105
Hirose, S., Blaes, O., Krolik, J. H., Coleman, M. S. B., & Sano, T. 2014, ApJ, 787, 1
Hirose, S., Krolik, J. H., & Stone, J. M. 2006, ApJ, 640, 901
Jiang, Y.-F., Stone, J. M., & Davis, S. W. 2014, ApJ, 784, 169
Ju, W., Stone, J. M., & Zhu, Z. 2016, ApJ, 823, 81
King, A. R., Pringle, J. E., & Livio, M. 2007, MNRAS, 376, 1740
Kotko, I., & Lasota, J.-P. 2012, A&A, 545, A115
Krolik, J. H., Hirose, S., & Blaes, O. 2007, ApJ, 664, 1045
Miller, K. A., & Stone, J. M. 2000, ApJ, 534, 398
O'Neill, S. M., Reynolds, C. S., Miller, M. C., & Sorathia, K. A. 2011, ApJ, 736, 107
Parker, E. N. 1955, ApJ, 122, 293
Rogachevskii, I., & Kleeorin, N. 2007, Phys. Rev. E, 75, 046305
Ruediger, G., & Kichatinov, L. L. 1993, A&A, 269, 581
Salvesen, G., Armitage, P. J., Simon, J. B., & Begelman, M. C. 2016a, MNRAS, 460, 3488
Salvesen, G., Simon, J. B., Armitage, P. J., & Begelman, M. C. 2016b, MNRAS, 457, 857
Shakura, N. I., & Sunyaev, R. A. 1973, A&A, 24, 337
Shi, J., Krolik, J. H., & Hirose, S. 2010, ApJ, 708, 1716
Shi, J.-M., Stone, J. M., & Huang, C. X. 2016, MNRAS, 456, 2273
Squire, J., & Bhattacharjee, A. 2015, Physical Review Letters, 115, 175003
Warner, B. 2004, PASP, 116, 115
Warner, B., & Woudt, P. A. 2002, MNRAS, 335, 84
Woudt, P. A., & Warner, B. 2002, MNRAS, 333, 411